Exploring The Excited-State Charge Transfer Fluorescence Profile of 7-Hydroxycoumarin and 2-Methylimidazole- A Combined X-Ray Diffraction and Theoretical Approach.

Bryson A. Hawkins,[1*] Elias Najib,[1] Jonathan J. Du,[2] Felcia Lai,[1] James A. Platts,[3] Paul W. Groundwater,[1] and David E. Hibbs.[1]

[1]*Sydney School of Pharmacy, Faculty of Medicine and Health, The University of Sydney, NSW 2006 Australia*

[2] *Department of Biochemistry, School of Medicine, Emory University, Atlanta, Georgia, USA.*

[3]*School of Chemistry, Cardiff University, Cardiff, CF10 3AT, UK*

**Corresponding author: Bryson A. Hawkins, bryson.hawkins@sydney.edu.au*

†Electronic supplementary information (ES) available. CCDC: 2155506, 2155508 and 2155507 for *(**1**), (2) and (3) For ESI and crystallographic data in CIF or other electronic formats, see DOI: XXXXXXX*

Abstract

This study investigated the effect of 2-methylimidazole (2MIM) addition on the fluorescence of ethyl-7-hydroxy-2-oxo-2*H*-chromene-3-carboxylate using low-cost density functional theory (DFT) and Time-Dependent DFT calculations on single crystal X-ray geometries of ethyl-7-hydroxy-2-oxo-2*H*-chromene-3-carboxylate hydrate (**1**), 2-MIM (**2**), and the 1:1 co-crystal of (**1**) and (**2**), (**3**). At low concentrations (1:1-1:10) of 2-MIM, the fluorophore shows a decrease in the fluorescence intensity, but at higher concentrations (above 1:10) the fluorescence excitation maximum shifted from 354 nm to 405 nm, with a significant emission intensity increase. The changed excitation and emission profile at high concentrations is due to the deprotonation of the coumarin's phenolic group, which was confirmed by the increased shielding of the aromatic protons in the titration ^{1}H NMR spectra. The experimental fluorescence data between the 1:1 and 1:10 ratios agreed with the theoretical fluorescence data, with a redshift and decreased intensity when comparing (**1**) and (**3**). The data indicated that combining the fluorophore with 2-MIM increased levels of vibronic coupling between 2-MIM and the fluorophore decreasing de-excitation efficiency. These increased vibronic changes were due to charge transfer between the fluorophore and 2-MIM in (**3**). The subtle movement of the proton, H(5) toward N(2') (0.07Å) caused a significant decrease in fluorescence due to electron density distribution (EDD) changes. This was identified by comparison of the EDD in the excited (S_1) and ground (S_0) states plotted as an isosurface of EDD difference. For the higher concentrations, an alternative excitation pathway was explored by modifying the crystal geometry of (**3**) based on ^{1}H NMR spectroscopy data to resemble excitoplexes. Theses excitoplex geometries reflected the fluorescence profile of the fluorophore with high concentrations of 2-MIM; there were dramatic changes in the theoretical fluorescence pathway, which was 100% vibronic coupling compared to 15.31% in the free fluorophore. At this concentration, the de-excitation pathway causes remodelling of the lactone ring *via* stretching/breaking the C=O bond in the S_1 causing increased fluorescence by movement of the transition dipole moment. These results reflect previous studies, but the methods used are less experimentally and computationally expensive. This study is among the first to explain charge transfer fluorescence using crystalline geometries. This study will be of interest to the fields of crystal engineering and fluorescence spectroscopy.

Introduction

Coumarins are highly versatile naturally occurring lactones with a wide range of applications, for example they are the primary backbone for vitamin K antagonists such as warfarin. However, they are also used as diagnostic tools due to the intense fluorescence they generate, [1-3] which has led to their use as biological, for example as probes for the rapid detection of bacteria when incorporated into aminopeptidase substrates.[4] Modulation of the fluorescence properties of 7-hydroxycomarins is possible, as previously demonstrated in studies by Chakraborty *et al*. and Amoruso *et al*., in which where the fluorescence of the hydroxycoumarin photoacid was altered by the introduction of an excited state charge transfer with colloidal silica and imidazole derivatives, respectively.[5, 6] The results of the study by Amoruso *et al*. indicated promise in the controlling the profiles of these fluorogens. [5-10]

Imidazole derivatives are bases and, as discussed by Amoruso *et al*., their deprotonation of the photoacid, 7-hydroxy-4-(trifluoromethyl)-1-coumarin leads to the amplification of its fluorescence.[5] It was shown in this study that the imidazole gained a proton from the photoacid through a bimolecular excited-state proton transfer. [5]

Although there have been many computational studies looking at photoacid stretch frequencies for heteroatom-H combinations in differing solvents, to achieve appropriate time-resolutions of the

excited-state proton transfer is computationally expensive.[11-13] As such, and shown by Amoruso *et al.*, systems, where the acid-base concentration can be controlled experimentally, application of complimenting computational methods on the various photoproducts generated can allow disentangling of biomolecular proton transfer states. However, Time-resolved Infrared Spectroscopy), as used by Amoruso *et al.,* is not easily performed, nor is it readily available in a general laboratory setting, leading to the need for alternative methods to identify or predict the potential excited-state proton transfer in photoacid systems. An argument can be made that utilizing a concentration gradient approach in the experimental fluorescence will result in the interaction of the coumarin and the methylimidazole in specific arrangements., which may be displayed in the ground state environment represented by a crystal structure. A 1:1 ratio of coumarin and imidazole could be the best representation of the interaction present between the fluorophore and the methylimidazole as it may be the most stable combination based upon Gibbs Free Energy, Ostwald's Step law and, Ostwald's ripening.[14-17] The crystalline geometry may thus be a good starting point for reviewing the fluorescence modulation resulting from the combination of the two agents .[18, 19] To do this the crystalline geometries are used as a starting point for the computationally cheap and less demanding theoretical calculations based upon first principles. [13, 20-22] Density Functional Theory (DFT) and Time-Dependent DFT (TDDFT) can be used to analyse the ground and excited state behaviour of the photoacid, and this is significantly less demanding than the use of high-resolution molecular dynamics.[13, 20-22] It is proposed that through this analysis of the ground-state electron density distribution (EDD), S_0, and that of the excited state, S_1, change in the photoacid created by the combination with imidazole derivatives on the basis of only simple standard resolution crystallographic data.[5]Herein, we report a study of ethyl 7-hydroxy-2-oxo-2*H*-chromene-3-carboxylate hydrate, (**1**), 2-methylimdazole, (**2**), and the combined 1:1 co-crystal of the two, (**3**), which are represented in Figure 3a-c, respectively. The results suggest that these techniques may benefit future studies of the modulation of other fluorophores through the combination of rational crystal engineering and low-cost computational calculations.

Methods

Single Crystals of ethyl 7-hydroxy-2-oxo-2*H*-chromene-3-carboxylate hydrate, (1), 2-methylimdazole, (2) and the co-crystal (3

For (1) the final product of synthesis (results) was dissolved freely in dichloromethane, (DCM), at room temperature (25°C), (0.002mol in 10mL DCM), it was left covered with a single piece of parafilm. Single crystals of (1) suitable for diffraction formed within 1 week. For 2-Methylimidazole, (**2**), it was purchased from Merck (Castle Hill, NSW) and was used without further purification. The co-crystal (**3**) was formed by combining equimolar amounts of (**1**) and (**2**), (0.002 mol) in DCM (10mL) at room temperature (25°C). The solute system was sealed with parafilm and allowed to evaporate at ambient conditions. Single crystal of (3) suitable for single crystal X-ray diffraction formed within a week. Information on crystal selection can be found in single crystal X-ray diffraction.

Single crystal X-ray diffraction

Single crystals of (**1**), (**2**) and (**3**) suitable for single-crystal X-ray diffraction (SC-XRD) were selected by hand using a rotating stage Olympus SZ61. The SC-XRD was carried out with each crystal mounted onto a thin-glass fibre with Paratone-N as an adhesive and cryoprotectant. The crystallographic analysis was carried out on an Agilent Supernova™ Diffractometer using MoKα (λ = 0.71073), with an Atlas CCD detector. The raw reflection data for all crystals were sorted and averaged using SORTAV by Blessing.[23] The structures were solved by intrinsic phasing using SHELX-T,

the subsequent independent atomic model (IAM) of each crystal then underwent a full-matrix least squared refinement on F^2 using SHELXL-2018.[24] The crystallographic structure of (**1**)-(**3**) are shown below in Figure 3 and selected crystallographic details for each crystal are given in Table 1.

Fluorescence studies

The fluorescence properties of (**1**) and the different molar ratios of (**1**) and (**2**) were performed in water on Shimadzu RF-5301PC spectrophotometer using a 5 mm slit width. The concentration of (**1**) was kept constant at 5μM and the concentration of (**2**) was increased to a maximum of 5mM. All collections were performed in triplicate, the fluorescence study was conducted in the same manner as that of the parent coumarin alone.

^{1}H NMR spectroscopy studies

The 7-hydroxycoumarin (**1**) (4 mg, 0.016 mmol) was dissolved in d_4-methanol (0.75 mL) and the ^{1}H NMR spectrum obtained on a Varian 400MR (Varian Australia Pty. Ltd., Mulgrave, Victoria, Australia) at 400 MHz; coupling constants (*J*) are in Hertz (Hz), chemical shifts (δ) are expressed in parts per million (ppm) and are reported relative to the residual solvent peak at 3.31 ppm. For (**2**) a sample of 4mg (0.049 mmol) was dissolved in d_4-methanol (0.75 mL) and the ^{1}H NMR spectrum was obtained in the same manner. For the titration, high concentration solutions of (**1**) and (**2**) were prepared in d_4-methanol (10mM and 100mM, respectively). The desired concentration ratio was combined and then diluted to a total volume of 0.75mL per sample. The ^{1}H NMR spectrum was obtained in the same manner as above. The 1H NMR spectrum of the phenoxide generated by the reaction of sodium methoxide and (**1**) was obtained by combining the in a 1:1 molar ratio in d_4-methanol (0.75mL).

Computational methods

For accurate theoretical calculations and modelling of the EDD, all covalent to hydrogen atom (X-H) bonds were fixed to averaged neutron data lengths reported by Allen *et al*.[25] The neutron corrected X-H (C_{ar}-H, C-H_2, C-H_3, N-H and O-H, were 1.083, 1.092, 1.059, 1.009 and 0.967Å, respectively) crystalline geometries of the asymmetric units and alternative bonding arrangement/dimers extracted from Mercury, were reviewed using ORCA 5.[26-28] The optimized ground state (S_0) geometries were obtained using the range-corrected hybrid functional ωB97XD and Def2-SVP basis set.[29-31] The optimized geometry of the first excited state (S_1) of each system was obtained using Time-Dependent DFT (TDDFT) using the same functional and basis set as the ground state. Both S_0 and S_1 geometries underwent harmonic frequency calculation to validate that the geometry was a true minimum on the potential energy surface. The DFT grid used was the default defgird2. This was deemed reasonable in the development of ORCA 5.0, as the numerical grid accuracy was enhanced by machine learning. [26-28] Defgrid 2 has been benchmarked against the GMTNK55 test set and all errors were systematically low for all computational determinants in the study. [26-28] The calculations of the theoretical fluorescence spectra were obtained by using TDDFT and the correlation functional within the ORCA_ESD module. [32] The spectra were obtained at the same functional as above, however, the basis set was escalated to Def2-TZVP to decrease the SCF energy error.[32] All calculations used a conductor-like polarized continuum model (CPCM) for water to reflect the experimental fluorescence conditions. [29, 33]

Table 1: Selected Physical Properties and Crystallographic Information for (**1**), (**2**) and (**3**).

	(**1**)	**(2)**	**(3)**
Formula	$C_{12}H_{10}O_5 \cdot H_2O$	$C_4H_6N_2$	$C_{12}H_{10}O_5 \cdot C_4H_6N_2$
Molecular Mass (g/mol)	252.22	82.10	334.32
Melting Point (°C)	166.1	142.4	156.2
Crystal size (mm)	0.14 x 0.15 x 0.55	0.3 x 0.2 x 0.6	0.6 x 0.3 x 0.16
Temperature (K)	139 (20)	150 (0)	120.15
Wavelength (Å)	MoKα (λ = 0.71073)	MoKα (λ = 0.71073),	MoKα (λ = 0.71073)
Crystal system	Triclinic	Orthorhombic	Triclinic
Space group	$P\bar{1}$	$P2_12_12_1$	$P\bar{1}$
a (Å)	6.65 (3)	6.02 (2)	7.51 (2)
b (Å)	7.11(3)	8.15 (4)	9.81 (3)
c (Å)	12.57(3)	9.69 (3)	11.11(2)
α°	103.59(3)	90	73.30(2)
β°	96.17 (3)	90	82.21(2)
γ°	98.82(4)	90	77.65(2)
Volume (Å^3)	564.74(4)	475.02 (0)	764.30(4)
Z	2	4	2
Refinement Method	full-matrix least squared refinement on F^2	full-matrix least squared refinement on F^2	full-matrix least squared refinement on F^2
No. of reflections Collected	12124	13019	58735
No. unique	12124	2246	12517
R_{int}	0.024	0.029	0.046
Completeness (%)	100	100	99.9
No. reflections used	2799	2246	12517
ρ_c (g cm^{-1})	1.48	1.15	1.37
F(000)	264.0	176.0	332.0
μ (mm^{-1})	0.12	0.075	0.10

$R(F)$, $R(F^2)$, all data	0.0395, 0.1058	0.058, 0.141	0.0431, 0.1137
Goodness of fit	1.046	1.041	1.036
Residual density (e Å^{-3})	-0.200, 0.440	-0.178, 0.507	-0.240, 0.610

Results

Synthesis and characterization of (1)

The synthesis of ethyl 7-hydroxy-2-oxo-2H-chromene-3-carboxylate (**1**) was achieved using an adaptation of the method of Ritter *et al*. summarised in scheme 1, (ESI). [34] The starting materials obtained from Merck (Castle Hill, NSW) were used without any further purification.[34] The final product (yield 24%) was characterised by NMR spectroscopy, mass spectrometry and single-crystal X-ray diffraction (SC-XRD), see ESI for NMR and MS data.

Fluorescence spectroscopy

As can be seen in figure 1a, the excitation wavelength maximum of (**1**) at 5 µM concentration is 354 nm and a smaller second excitation maximum of 408 nm. It is seen that the excitation spectra displayed progressive red shifts with increasing concentrations of (**2**) up to a ratio of 1:10, with the intensity decreasing and a shift in the maximum of by 16 nm, to 370 nm, in the 1:10 solution. Significantly, this solution displays two excitation maxima, and at concentration ratios of 2-MIM exceeding 1:10, there is a clear variation in the excitation profile of the fluorophore with an increase in intensity and by 1;100 the excitation maximum at. This causes a large increase in fluorescence emission, as depicted in Figure 1b, due to the excitation profile being completely different at the high concentration ratio (>1:10) as a result of phenol becoming deprotonated; rather than exciting (**1**) it is the phenoxide equivalent of the 7-hydroxycoumarin which is excited, which requires a larger excitation energy wavelength as reflected in Figure 1a. As expected, the excitation of the phenoxide rather than the phenol is associated with a significant increase in the fluorescence intensity, which is well known to occur in high pH environments.[35] To confirm the phenoxide formation, a ^{1}H NMR spectroscopy study of the titration of 7-hydroxycoumarin (**1**) against 2MIM (**2**) in d_4-methanol was undertaken, Figure 2. As can be seen from Figure 2, increasing the ratio of 2MIM to the 7-hydroxycoumarin, from 1:1 to 1:10 to 1:100, results in increased shielding of the signals for H-4, H-5, H-6 and H-8, as would be expected for the formation of the phenoxide and the resulting increased electron density in the aromatic rings.[36] For comparison, the ^{1}H NMR spectrum of the fluorophore (**1**) after treatment with NaOMe / d_4-methanol was obtained and this confirms the shielding of the protons on both rings, particularly H-5,H-6 and H-8, demonstrating the increased electron densities at these positions.

Figure 1b shows the emission profile, the emission wavelength maximum of (**1**) at 5 µM concentration is 445 nm and remains unchanged on treatment with the range of concentrations of (**2**). However, a decrease in fluorescence intensity is seen with increasing concentrations of (**2**) up to a ratio of 1:10, whereupon it increases dramatically once the concentration ratio is >1:10. At the high concentration ratios (>1:10) there is no change in the emission wavelength which, in addition to the different excitation profiles, indicates that at a certain ratio the fluorophore structure no longer equilibrates and de-excites via non-radiative decay; a new de-excitation pathway occurs in the anion

form, as was seen in the work of Chowdhury *et al.*, where the deprotonation of the fluorophore resulted in a magnitude increase in fluorescence.[21] However, at the low concentration ratios, the spectra reflect what has been seen previously, with a small redshift and decreased fluorescence.[5]

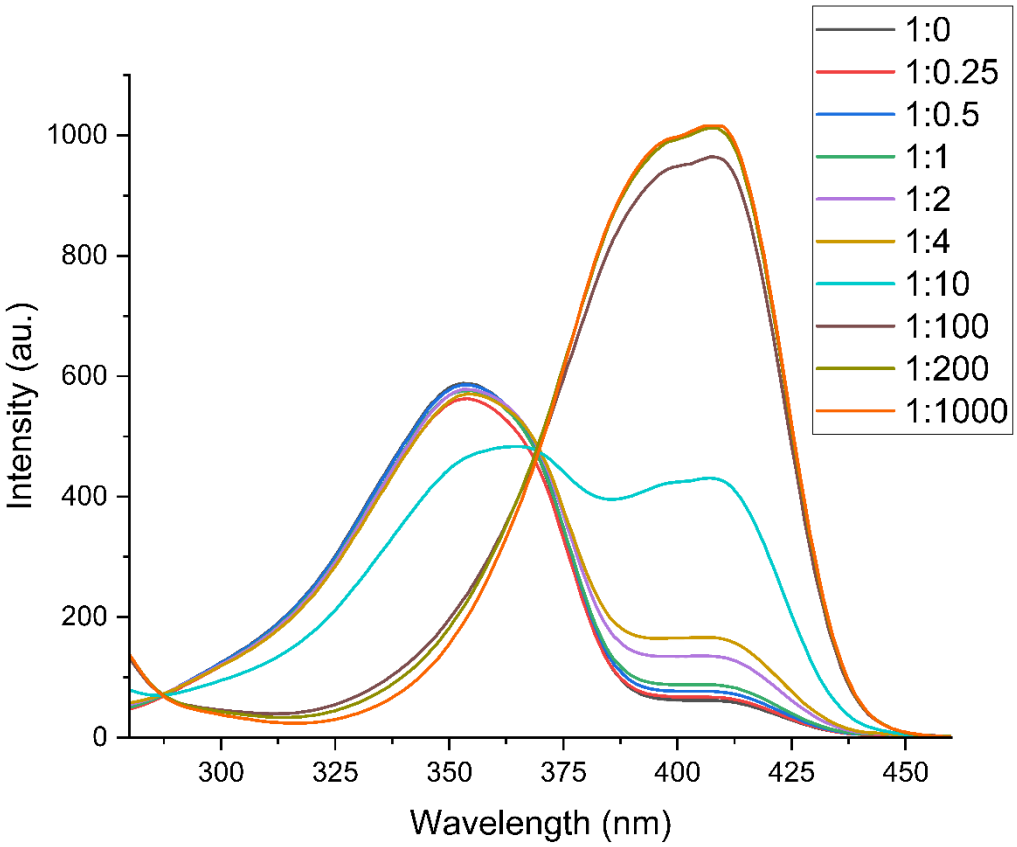

(a)

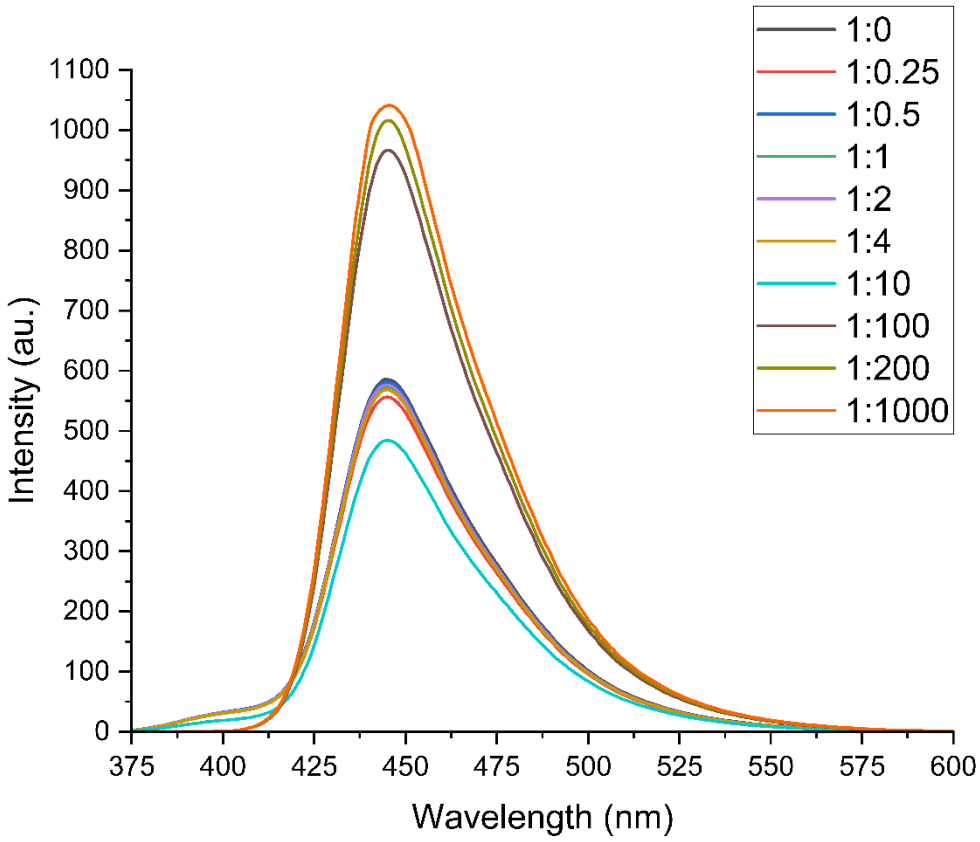

(b)

Figure 1: (a) Excitation spectrum of (**1**) at 5 µM with differing concentrations of (**2**) in water. Fluorescence intensity (a.u.) plotted against emission wavelength (nm). (b) Emission spectrum of (**1**) at 5 µM with different concentration ratios of (**2**) in water. Fluorescence intensity (a.u.) plotted against emission wavelength (nm).

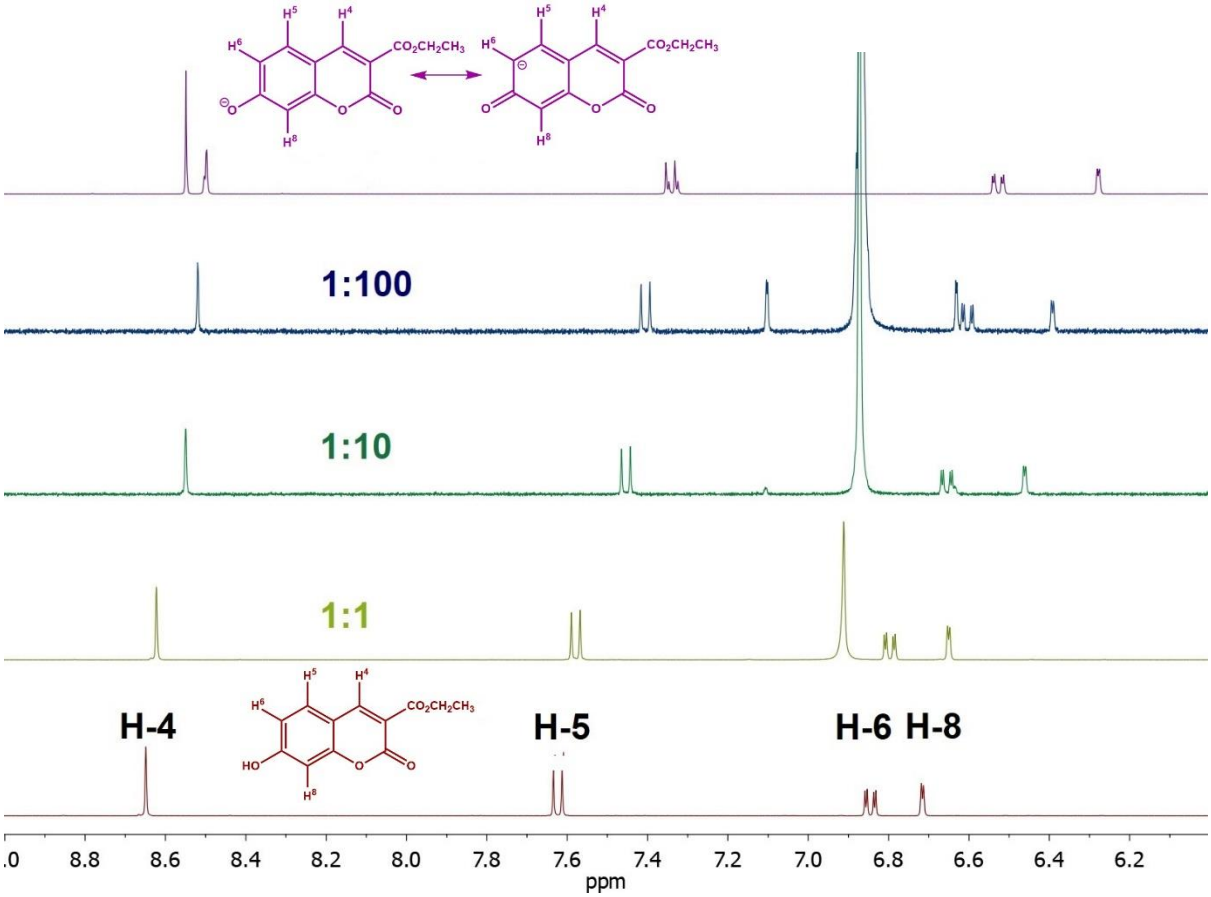

Figure 2. ^{1}H NMR titration of 7-hydroxycoumarin (**1**) against 2MIM (**2**) in d_4-methanol, showing ratios of (**1**):(**2**). All spectra are referenced to the signal for the partly deuterated solvent (δ3.31)

Crystallographic Analysis

X-ray diffraction provided clear evidence for the final product of (**1**), and (**2**) and the formation of (**3**). Selected X-ray diffraction results are reported in Table 1 and hydrogen bonding information can be found in Table 2. For (**1**), Figure 3a, the final crystallized product was a hydrate with a conventional hydrogen bond forming with the phenol and the water molecule, (O(5)-H(5)⋯O(1'). The crystal packing for (**1**) represents a 2,2,1(s) configuration with an aromatic cycle system between coumarin moieties stacked in an antiparallel manner.[37] For (**1**), the extracted bonding arrangements include the asymmetric unit, a bifurcated hydrogen-bonding system in the -x+2, -y+1, -z+1 symmetry operator plane, as well as the antiparallel cycle stack (Figure 4a,b, and c respectively). For (**2**), Figure 3b, the unit cell is held together by a single conventional hydrogen bond extending outside of the unit cell between the pyrrole and pyridine nitrogen atoms, (N(1')-H(1'A)⋯N(2'), -x +3/2, -y+1, z-1/2 symmetry operator plane. For (**2**) the packing arrangement is a 2,2,1(m) appearance with no aromatic cycle stack between 2MIM moieties. [37] For (**2**) other than the single 2-MIM moiety, a dimer was generated which is formed by the pyrrole and pyridine hydrogen bond (represented in figure 4d). For (**3**), Figure 3c, the asymmetric unit consists of a 1:1 stoichiometry of 2MIM and the coumarin moieties, the cell is maintained by a conventional hydrogen bond between the phenol and pyridine nitrogen species, (O(5)-H(5)⋯N(2'). The packing of (**3**) resembles a 2,2,1(s) arrangement with a possible aromatic cycle stack between the coumarin and 2-MIM moieties, as seen fixed along the b-axis depicted 4g, dimer **3.c**. [37] The extracted dimers for (**3**) also include the unit cell bonding

arrangement and the bifurcated hydrogen-bonding system in the x-1, y+1, z-1 symmetry plane (Figure 4 e and f). Interestingly it can be seen that in (**1**) and (**3**) the hydrate and 2MIM hydrogen bond in the same locations on the coumarin with the phenol donated hydrogen bond and the bifurcated hydrogen bonds from the lactone ring.

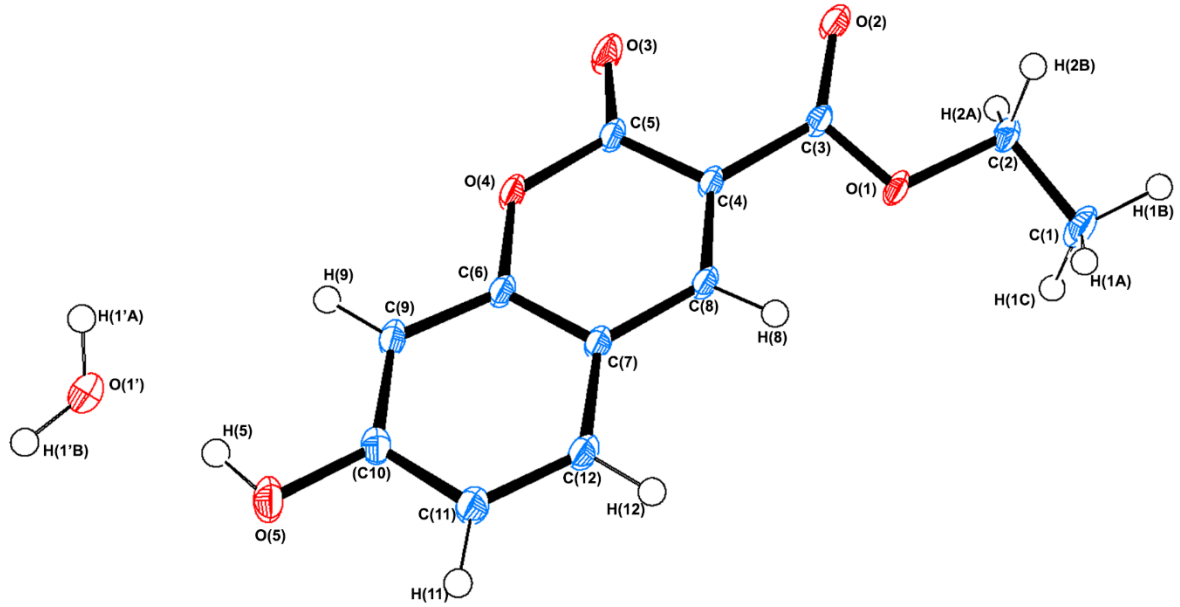

(a)

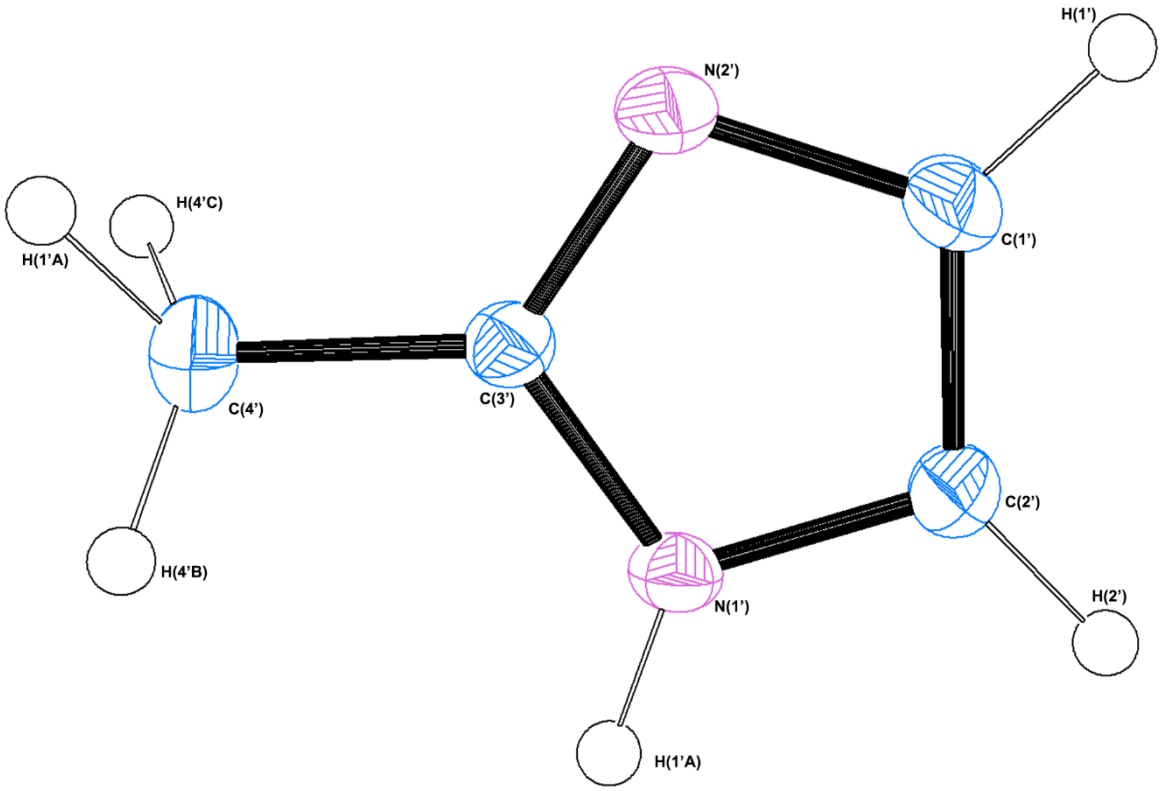
H(1')
N(2')
H(4'C)
H(1'A)
C(1')
C(4')
C(3')
C(2')
H(4'B)
N(1')
H(2')
H(1'A)

(b)

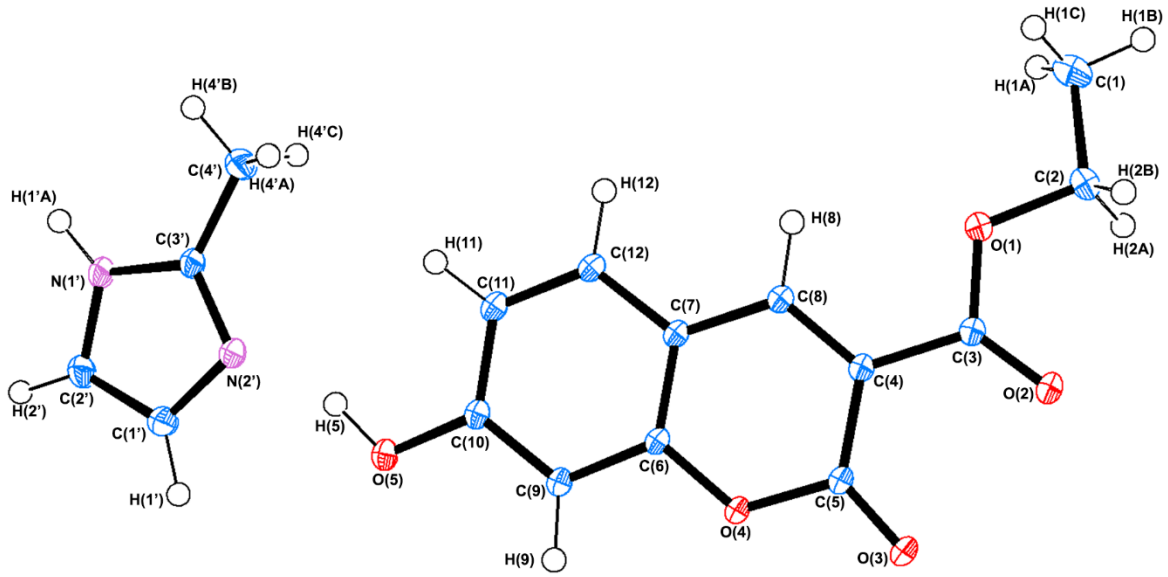
H(1C)
H(1B)
H(4'B)
H(1A)
C(1)
H(4'C)
C(4')
H(4'A)
C(2)
H(2B)
H(1'A)
H(12)
H(8)
C(3')
H(11)
O(1)
H(2A)
N(1')
C(12)
C(11)
C(7)
C(8)
C(3)
N(2')
C(4)
O(2)
H(2')
C(2')
H(5)
C(10)
C(1')
C(6)
O(5)
C(9)
C(5)
O(4)
H(1')
O(3)
H(9)

(c)

Figure 3: ORTEP probability plots of the IAM of (**1-3**), (a-c), respectively. Thermal ellipsoid probability set to 50%.[38]

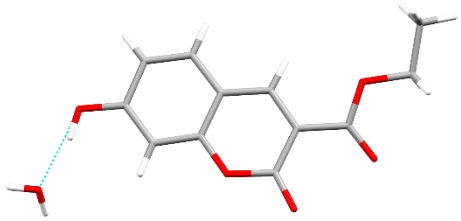

(a)

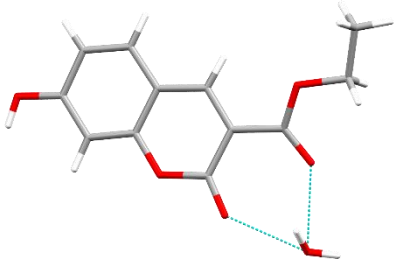

(b)

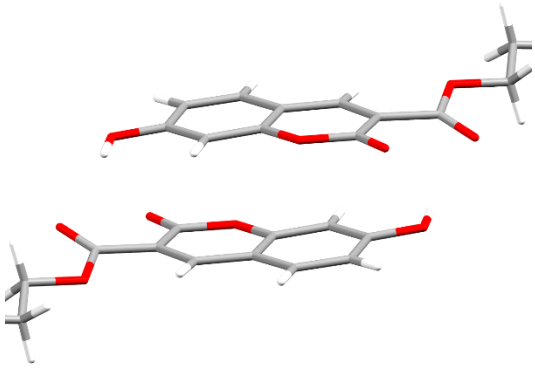

(c)

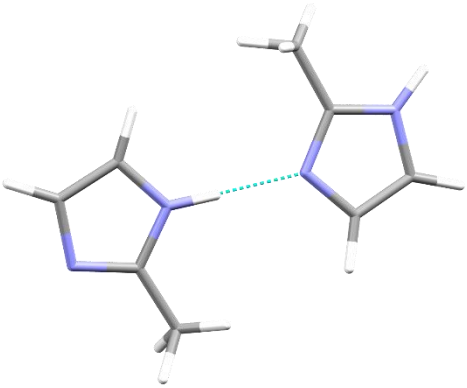

(d)

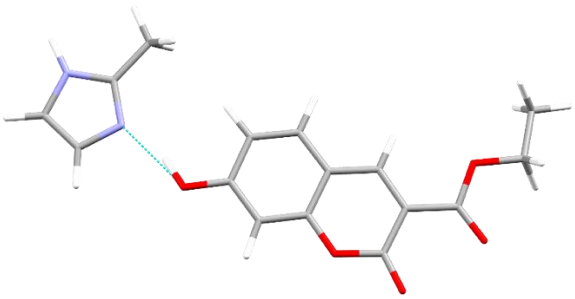

(e)

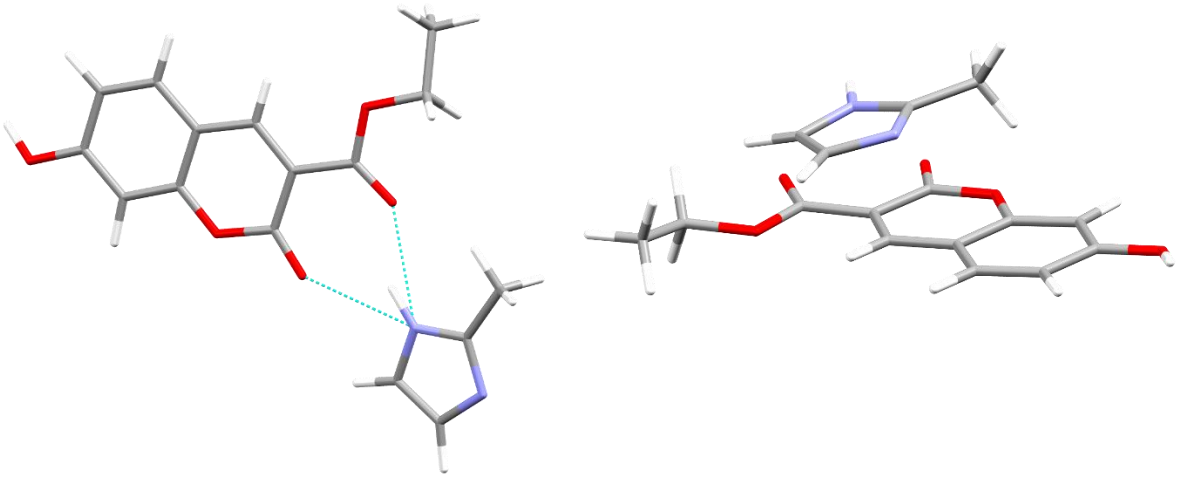

(f) (g)

Figure 4: Selected dimer arrangements from crystallographic geometries, naming scheme and description of dimer. Naming of dimers for the reminder of the paper is summarized here. For each dimer No.x, where the number (No.) is the crystal of reference and the letter (x) is a, *etc*., is the dimer orientation in this figure. As such, for (**1**), Ethyl 7-hydroxy-2-oxo-2H-chromene-3-carboxylate hydrate, (a) (**1.a),** hydrate dimer asymmetric unit orientation. (b) (**1**.b), hydrate dimer extending outside the asymmetric unit on in the -x+2, -y+1, -z+1 symmetry operator plane. (c) (**1.c**), aromatic cycle stack orientation, stack identified in the 1-x,1-y,1-z symmetry operator plane. For (**2**), 2-MIM, (d) (**2**.a), Dimer of 2-MIM extending outside of asymmetric unit, -x +3/2, -y+1, z-1/2 symmetry operator plane. For (**3**), Ethyl 7-hydroxy-2-oxo-2H-chromene-3-carboxylate:2-MIM, (e), (**3**.a) Fluorophore:2-MIM asymmetric unit orientation. (f), (**3**.b), Fluorophore:2-MIM dimer extending outside the asymmetric unit on in the - x-1, y+1, z-1 symmetry operator plane. (g), Fluorophore:2-MIM aromatic cycle stack orientation, stack identified in the 1-x,2-y,1-z symmetry operator plane.

Table 2: Hydrogen bond present in (**1**), (**2**) and (**3**).[28]

System	**Donor Atom – Hydrogen Atom Length (Å)**	**Hydrogen Atom – Acceptor Atom Length (Å)**	**Donor Atom – Hydrogen Atom – Acceptor Atom Angle (°)**	**Symmetry Operator**
(**1**)				
O(5) – H(5) ⋯ O(1’)	0.820	1.671	171.70	n/a
O(1’) – H(1’A) ⋯ O(2)	0.885	2.308	170.58	x, y, z-1
O(1’) – H(1’B) ⋯ O(2)	0.830	2.096	140.47	-x+2, -y+1, -z+1
O(1’) – H(1’B) ⋯ O(3)	0.830	2.459	141.93	-x+2, -y+1, -z+1
(**2**)	**Donor Atom – Hydrogen Atom Length (Å)**	**Hydrogen Atom – Acceptor Atom Length (Å)**	**Donor Atom – Hydrogen Atom – Acceptor Atom Angle (°)**	**Symmetry Operator**
N(1’) – H(1’A) ⋯ N(2’)	0.975	1.842	179.32	-x +3/2, -y+1, z-1/2

(**3**)	**Donor Atom – Hydrogen Atom Length (Å)**	**Hydrogen Atom – Acceptor Atom Length (Å)**	**Donor Atom – Hydrogen Atom – Acceptor Atom Angle (°)**	**Symmetry Operator**
O(5) – H(5) ⋯ N(2')	0.987	1.643	162.04	n/a
C(9) – H(9) ⋯ O(5)	1.009	2.436	167.77	-x+1, -y+1, -z+1
N(1') – H(1'A) ⋯ O(2)	0.919	2.036	150.12	x-1, y+1, z-1
N(1') – H(1'A) ⋯ O(3)	0.919	2.209	127.99	x-1, y+1, z-1
C(4') – H(4'B) ⋯ O(2)	0.993	2.479	138.87	x-1, y+1, z-1

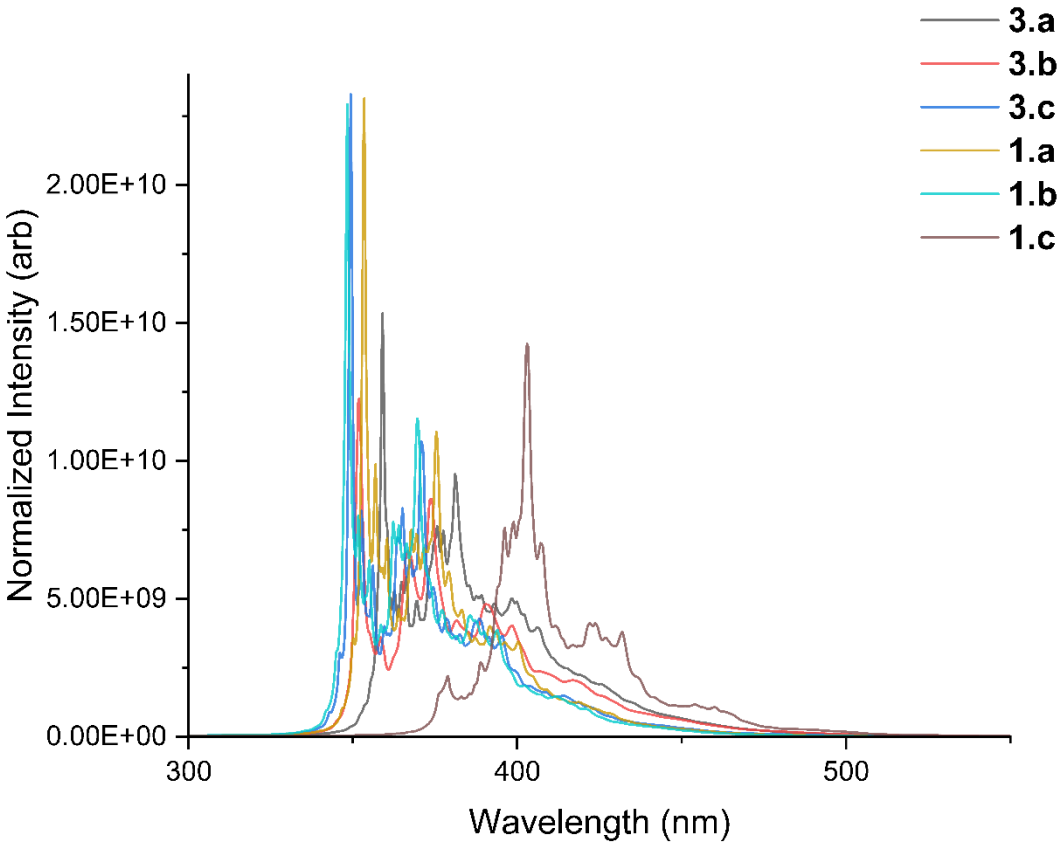

(a)

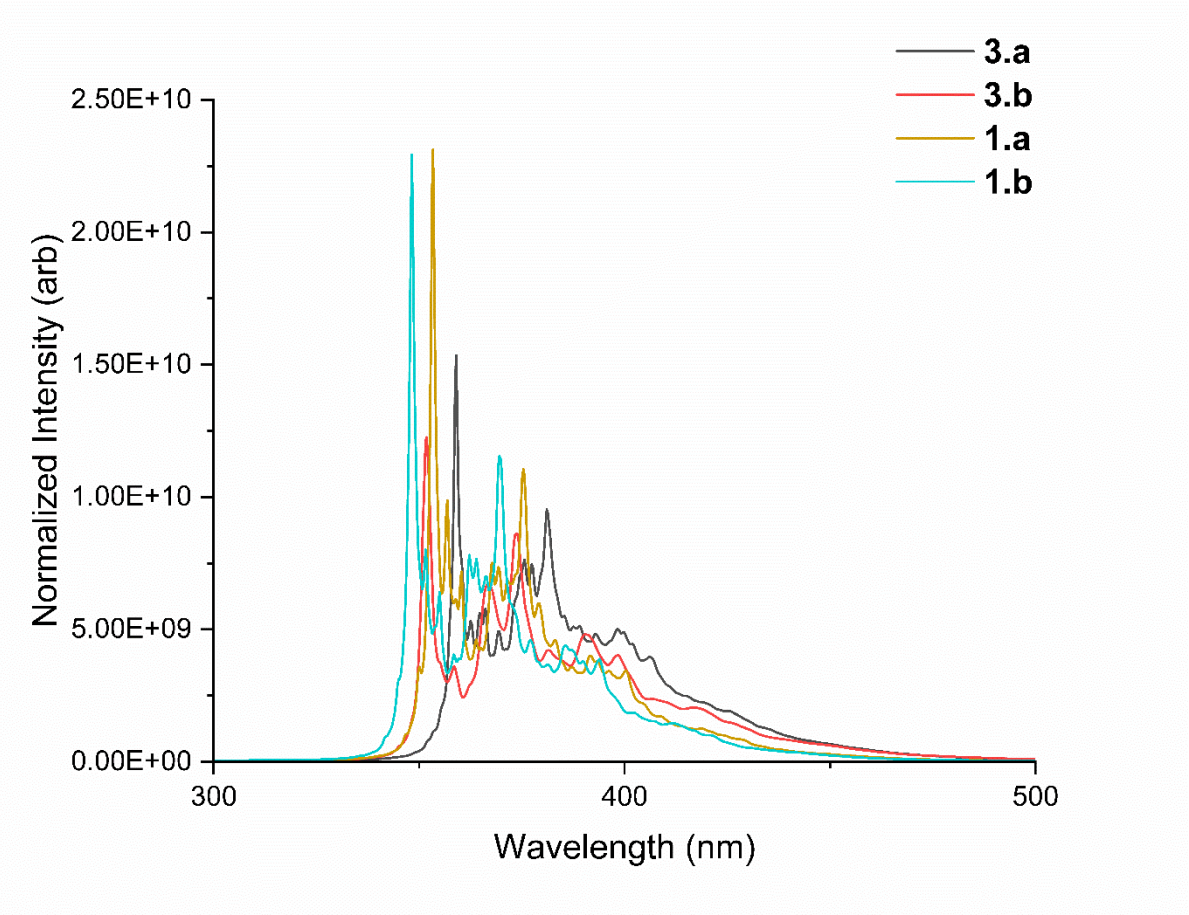

(b)

Figure 5: (a)Combined theoretical fluorescence spectra of all dimer combinations for (**1**), and (**3**) all calculated in water using ORCA_ESD.[27, 38] (b) theoretical fluorescence spectrums of (**1.a**), (**1.b**), (**3.a**) and (**3.b**) extracted from Figure 5a for further clarity of properties.

Table 3: Selected fluorescence properties from the ORCA_ESD calculations for (**1**) and (**3**).

Compound	**Adiabatic Energy Difference** cm^{-1} / nm	**Fluorescence Rate Constant** (k_f) (s^{-1*})	Franck-Condon %	Herzberg-Teller %
(1.a)	28301 / 353.3	9.55×10^8	84.69	15.31
(1.b)	28716 / 348.2	9.60×10^8	84.35	15.65
(1.c)	26493 / 377.5	7.64×10^8	0.00	100.0
(3.a)	27857 / 359.0	9.91×10^8	82.05	17.95
(3.b)	28433 / 351.7	9.08×10^8	83.23	16.77
(3.c)	28630 / 349.3	9.13×10^8	84.45	15.55

Figure 5 shows the theoretical fluorescence plots for the solvated monomer (2-MIM only) and dimer combinations as described in detail above (Figure 4). For assisting in understanding the theoretical fluorescence data, the corresponding adiabatic energy differences, fluorescence rate constants (k_f, Franck-Condon (FC %) and Herzberg-Teller (HT %) are summarized in Table 3. The adiabatic energies ($\Delta\ U$) differences show the work performed between the S_1 and S_0 potential energy surfaces, the

information provided from ΔU (and its inverse) can indicate the potential energy release from the $S_1 \rightarrow S_0$ de-excitation. The k_f indicates the lifetime of the S_1 before deactivating to the S_0 *via* nonradiative decay, as such indicating how long the fluorophore should be fluorescent for, this will provide information on how the introduction of 2-MIM to the fluorophore affects the fluorescence lifetime.[40] The Franck-Condon percentage indicates the overlap of electronic wavefunctions between initial and final states, providing information on how similar the excitation state is to the ground-state. Simply, the larger the FC % the smoother energetic transition from S_1 to S_0. [41] Lastly, the HT %, the Herzberg-Teller effect indicates the portion of the fluorescence spectra caused by vibronic coupling derived by the expansion of the transition dipoles over the nuclear coordinates.[32] In the fluorophore here showed the HT % was significantly limited, ~15%, correlating with previous results for 7-hydroxycoumarin.[5, 42]

Firstly, it is evident that the theoretical fluorescence plots correlate with the experimental data (Figure 1), where the 1:1 ratio crystallographic structure of 2-MIM and fluorophore mimics the experimental data between the 1:0-10 concentration ratios, causing a redshift and decrease in observed fluorescence. It is evident that (**1**)'s fluorescence is unadjusted in a hydrate form; this is reflected by both (**1.a**) and (**1.b**) being practically equal in intensities across the plot, and their k_f being near-identical (9.60 x 10^8 s^{-1*} vs. 9. x 10^8 s^{-1*}, for (**1.a**) and (**1.b**), respectively). This is also reflective of the ΔU being negligible between (**1.a**) and (**1.b**) (28301 vs. 28716 cm^{-1}, respectively). The FC % and HT % are essentially equal, within 0.4% (Table 3), suggesting the hydrogen bonding of water to the fluorophore at either coordination point does not interfere with the vibronic coupling of the $S_1 \rightarrow S_0$ states.

From the plot is seen that (**3.c**) resembles a similar theoretical fluorescence as (**1.a**) and (1.b), this is most likely to due to the ΔU of (**3.c**) 28630 cm^{-1} is near equal to what is seen in (**1.a**) and (1.b). Furthermore, the k_f is 9.13 x 10^8 s^{-1*} for (**3.c**), this is like the relationship seen above in ΔU for (1.a) and (1.b). An explanation for this is that the geometry of (**3.c**) does not involve the same coordination points for hydrogen bonding compared to what is seen in (**1.a**) and (**1.b**) for (**1**) and (**3.a**) and (**3.b**) for (**3**) discussed above. This suggests that the EDD of the 2-MIM fragment does not interfere with the EDD of the fluorophore coumarin, as such the EDDs correlation of the S_0 and S_1 wavefunctions is unimpeded. This is also reflected in Table 3, where the FC % and HT % for the dimer (**3.c**) are ~0.2% varied from dimers (**1.a**) and (**1.b**). This indicates that 2-MIM does not change the energy route for the $S_1 \rightarrow S_0$ deexcitation in (**3.c**). Thus, this allows for the de-excitation of $S_1 \rightarrow S_0$ to occur as efficiently as in forms (**1.a**) and (**1.b**).

The decreased fluorescence is evident in the ΔU for (**3.**a) being significantly lower than the free form fluorophore (27858 cm^{-1}), this, however, was not as clear for (**3.**b), (28434 cm^{-1}), this ΔU is a comparable energy difference to what is seen in the arrangements of (1.a) and (1.b). This suggests that the ΔU alone is not powerful enough to explain the efficiency of deexcitation from $S_1 \rightarrow S_0$. However, the FC % and HT % relationship indicates that both (**3.a**) and (**3.b**), have a decreased excitation well overlap due to a small increase in the percentage of vibronic coupling between excited and ground-state wavefunctions (Table 3). Although the FC % decreases by a small amount (~2 % and ~1 %, in (**3.a**) and (**3.b**), respectively), it highlights that the addition of the 2-MIM creates a less efficient overlap $S_1 \rightarrow S_0$ wavefunctions in (**3**) resulting in the decreased fluorescence for both orientations. As the HT % indicates the level of difference in the excited and ground states wavefunctions, the minor increase may indicate a possible excited-state proton transfer, which has been well seen for this class of fluorophores.[5, 6, 42, 43]

Overall, the theoretical fluorescence spectra generated identified that the decreased fluorescence is caused by reduced overlap between the S_1 and S_0 wavefunctions. This creates a decreased intensity and moderate redshift of the fluorophore when comparing (**1**) and (**3**). This variation between (**1**) and (**3**) is due to the electron-withdrawing behaviour of N(2') from 2-MIM on the acidic phenol

region of the fluorophore. As the crystallographic geometries showed the hydrogen bonding environment of the (**1**) and (**3**) to be remarkable similar reviewing the bonding distance in the S_1 and S_0 may be a good starting point for understanding the modulation of the fluorophore.

As seen above, in the theoretical fluorescence data the effective overlap of the $S_1 \rightarrow S_0$ de-excitation is vital for creating optimal fluorescence. However, adding 2-MIM to the fluorophore affects this overlap. Identification of the decreased wavefunction overlap location will provide information on how the modulation of the fluorescence occurred. One simple way to attempt to identify this location is to simply look at geometrical changes that occur between the S_0 and S_1 wavefunction. Looking at the Root Square Mean Displacement of atomic positions between S_0 and S_1 in each monomer or dimer it highlights most prominently geometrical displacement for all bonds and angles was in seen in the (**2.a**), with a RMSD of 0.2 Å. However, when reviewing (**3.a**), it was clear that there was a displacement of the hydrogen atom in the phenol moiety, where it shifted 0.07 Å towards the 2-MIM fragment in the S_1. This is a very small movement of the proton, which does not necessarily indicate proton transfer, however, it may indicate a level of excited-state charge transfer between the 2-MIM and fluorophore fragment in line with other coumarin studies.[44] This suggests that geometrically this very subtle change that the overlapping of the EDD between S_0 and S_1 varies correlating to the HT % increase seen by 2-MIM addition in (**3.a**). A method to review this is to plot an isosurface of $\Delta\rho$ between the optimized energy states, which is summarized by equation 1 below, the calculation was performed using Multiwfn.[45]

$$\Delta\rho = \rho_{S_1} - \rho_{S_0} \quad (1)$$

The points of the plotted isosurface will indicate the difference in the EDD between S_0 and S_1, where if the fluorophore fragments have a minimal change *i.e.* less prominent isosurface it indicates a better overlap of the excited and ground-state wavefunction. These isosurfaces are represented in Figure 6.

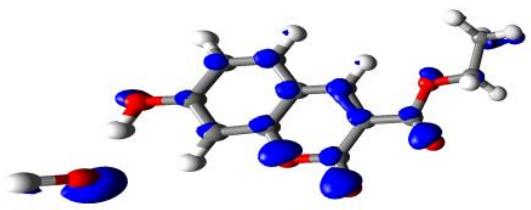

(a)

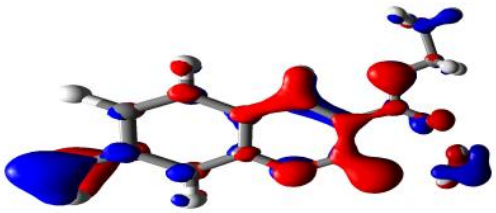

(b)

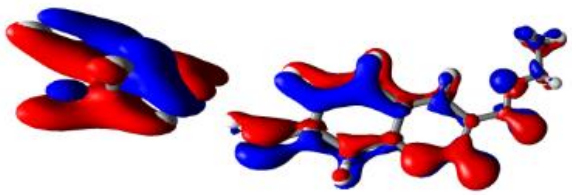

(c)

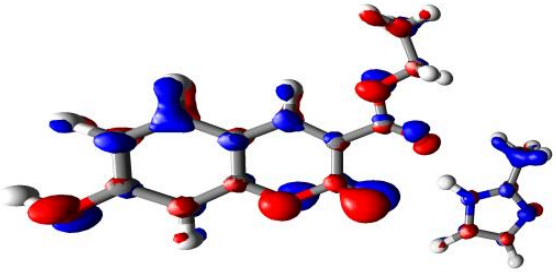

(d)

Figure 6: $\Delta\rho$ $S_1 - S_0$ isosurface plots of the coordination dimers. Plotted at $\pm$ 0.05e, positive *e* changes represent in red, negative changes represented in blue. (a) (**1.a**) (b) (**1.b**), (c) (**3.a)**, and (d) (**3.b**).[45, 46]

From Figure 6c it is clear that the $\Delta\rho$ $S_1 - S_0$ is most pronounced in (**3.a**), with large variations in ρ caused by the movement H(5) in the excited state to from the oxocoumarin moiety to 2-MIM. The large changes are indicated on the isosurface with changes on both 2-MIM and the fluorophore fragment. Interestingly, here it is shown that the oxocoumarin fragment has larger visual changes compared to figure 6a, representing (**1.a**), which indicates that 2-MIM gaining more charge from H(5) impedes the efficiency of deexcitation by creating a worse overlap in the wavefunction of S_1 and S_0 (3.a) leading to a reduced fluorescence as clearly seen above (Figure 5 and Table 3).

The other plots here also agree with the theoretical fluorescence spectrums for (**1.a**) and (**1.b**). It is seen that there is minimal change in the $\Delta\rho$ $S_1 - S_0$ of the fluorophore suggesting that water binding to the fluorophore's hydrogen bond coordination points does not impede the de-excitation of states, hence not changing the observed fluorescence. For (**3.b**) there is a slightly more pronounced variation in $\Delta\rho$ $S_1 - S_0$ in the oxocoumarin fragment only, suggesting that is coordination point in the lactone region does not cause such a heavy reduction in fluorescence unlike what is seen in (**3.a**). Comparing these (**3.a**) with (**3.b**), only (**3.a**) has a level of excited-state charge transfer, whilst (**3.b**)'s bifurcated hydrogen bond arrangement does not move at all between S_0 and S_1 (1.025 v. 1.027 Å, respectively).

The subtle charge transfer in (**3.a**) results in the phenol of the oxocoumarin fragment being more deprotonated in the S_1. This results in a larger equilibrium percentage of phenoxide formation in the S_1. This causes more electron density to be pushed into the π-system of the fluorophore, which is well known to cause a redshift. [6, 43, 47] A logical way to identify electron density movement or possible charge transfer is the application of Bader's Quantum theory of atoms in molecules (QTAIM).[48] The QTAIM was performed using the wavefunctions determinates of the respective dimers at their optimised state (as per method sections, ωB97XD/Def2-SVP). The QTAIM calculations were performed using the AIMALL suite by Keith.[49]

As such, QTAIM was applied in (**3.a**)'s S_0 and S_1 completeness of the investigation indicated by fulfilment of the Poincaré-Hopf theorem. Similarly, plots of ρ and $\nabla^2\rho$ (figure 7) along with the O(5)-H(5)⋯N(2') within (**3.a**) in the S_0 and S_1 state show movement of H(5) of 0.07 Å towards the 2-MIM fragment in S_1 with clear electron density movement. The hydrogen bond between the fragments gains 0.25 e $Å^{-3}$ (at the H(5) ⋯ N(2') BCP) in the excited state (0.44 v. 0.69 e $Å^{-3}$, S_0 and S_1 respectively), conversely, it is shown that the O(5)-H(5) BCP loses 0.36 e $Å^{-3}$ between states (1.94 v. 1.57 e $Å^{-3}$, S_0 and S_1 respectively). This shows that the H(5) EDD is shared in both states, obviously as they are hydrogen bonded together. However, in S_1's EDD the H(5)'s is positioned slightly more towards the 2-MIM fragment.

This movement of EDD disrupts the EDD equilibrium in S_1, and one method to review this concept is the analysis of interfragment charge transfer amount.[45] The method indicates the movement of charge between each fragment, it also indicates intrafragment redistribution of charge. Separating (**3**) into the fluorophore and 2-MIM fragments respectively, it is seen that 0.01 e is gained by the 2-MIM fragment, conversely, the fluorophore loses the same. Although this is a tiny amount of an electron density, it causes a large 0.99 e redistribution of the intrafragment charge of the fluorophore, this is most likely the movement from π to π^* as seen in other studies.[44] However, alongside the $\Delta\rho$ $S_1 - S_0$ isosurface of (**3.a**) it shows this redistribution is heavily distorted across the whole system corresponding with a decreased energy well overlap shown by FC % findings above. This means the system is trying to equilibrate the intrafragment charge movement across the whole molecule and in turn in the photoacid not efficiently emitting the energy as fluorescence. The re-establishment of the EDD equilibrium is predicted to be hampered by the electron density being

pushed back towards the phenoxide moiety in S_1. When reviewing the C(10)-O(5) BCP, it is seen that it gains 0.11 e Å^{-3} (2.15 v. 2.26 e Å^{-3}, S_0 and S_1 respectively), correlating to the $\Delta\rho$ $S_1 - S_0$ across the whole wavefunctions and the FC % changes. This is larger than that seen across the same bonds in (**1.a**) where overall electron density in the phenol fragment remains predominantly unadjusted between states (0.33 v 0.38 e Å^{-3} for the O(5) -H(5) ⋯ O(1') and the C(10) – O(5) 2.11 v 2.18 e Å^{-3}, in the S_0 and S_1, respectively). Similarly, this is reflected in the interfragment charge transfer review, where no EDD is moved between the fluorophore and the water molecule. However, there is also a 0.99 e intrafragment charge redistribution in the fluorophore, which is also the movement from π to π^*, however, when correlated to Figure 6a it can be visually seen that the movement between S_1 and S_0 is smoother, and results in a more favourable de-excitation. Overall, it is shown that the use of $\Delta\rho$ $S_1 - S_0$ isosurface review, interfragment charge transfer analyses and topology indicated that the fluorophore undergoes subtle charge transfer in the excited state of (**3.a**), caused by the movement of BCP location of the hydrogen increasing the EDD in the oxocoumarin fragment as the phenol resembling more of a phenoxide moiety in the S_1.

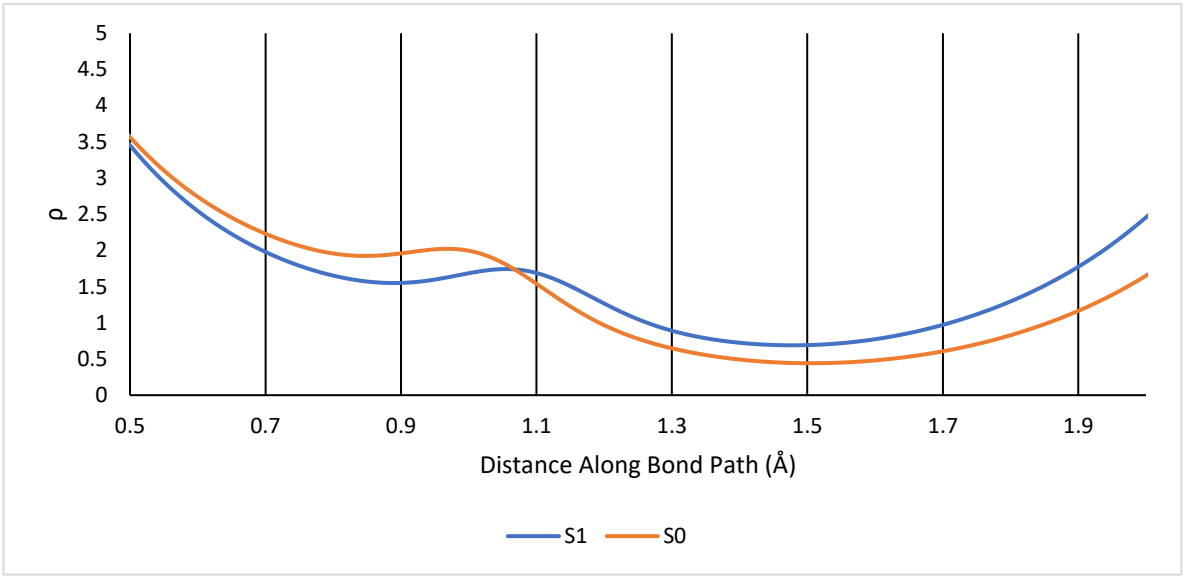

(a)

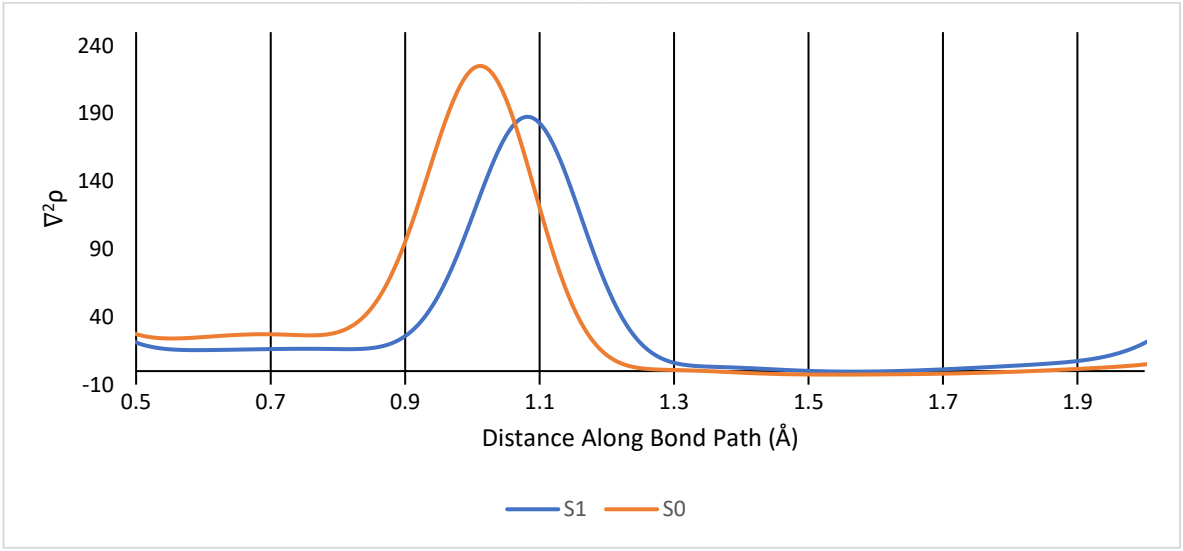

(b)

Figure 7: ρ (a) and $\nabla^2\rho$ (b) of the O(5)-H(5)⋯N(2') bond trajectory in S_0 (orange) and S_1 (blue), the bond path has been contracted by 0.5 Å in both directions toward H(5) to remove the core contributions of O(5) and N(2').

However, from the above, the theoretical fluorescence work could not identify the secondary excitation trend from the experimental data. This is due to the increasing concentration gradient forcing complete deprotonation of the fluorophore, which was confirmed by the titration ^{1}H NMR study. The ^{1}H NMR study indicated at high concentration ratios above 1:10 the coumarin's phenol deprotonates creating an anion equivalent. Using the ^{1}H NMR data, and the proposal of an excitoplex arrangement by Amoruso *et al,* can be attempted by generating excitoplexes from the crystallographic data.[5] **3.**a. was selected as it is the most likely to form first based on the data above that shows the proton movement in S_1 wavefunction, this was absent in **3.b.** The concept of **3.c.** is based on the work of Amoruso *et al*. directly, as in their study they alluded to a geometrical arrangement of aromatic cycle stack between the 7-hydroxycoumarin anion and methylimidazole cation forms.[5] This conceptual excitoplex was not formally characterized in their study. [5] To modify **3.a.** and **3.c.** the coumarin is converted to an anion form by removing the proton H(5) from the phenol O(5) and adding it to N(2') of 2-MIM, to produce a cation form using Avogadro, the excitoplexes are visualized below in Figure 8. To ensure the chemical relevancy of each excitoplex form the S_0 and S_1 geometries were optimized at ωB97XD functional and Def2-SVP, each of which underwent numerical frequency review to ensure the states were not an imaginary point on the SCF.[29,30] The excitoplexes, may correlate with the experimental fluorescence curve at high concentrations >1:10 where the excitation profile significantly varied, and emission was enhanced significantly. This would follow other studies whereby full deprotonation of the fluorophore resulted in significant fluorescence modulation.[7-9, 21, 50] Alongside Figure 8's representations of the excitoplexes (a and b for 3.a-excitoplex and 3.c-excitoplex, respectively) (c) and (d) are the $\Delta\rho$ $S_1 - S_0$ isosurface plots (e) is the theoretical fluorescence spectra. Table 4 summaries the selected fluorescence data from the ORCA_ESD calculations.[32]

Figure 8a and 8c show the **3.a-exctoplex**'s geometry and $\Delta\rho$ $S_1 - S_0$ isosurface, respectively. For the **3.a-excitoplex** the theoretical fluorescence plot (Figure 8e) shows a dramatic increase in overall intensity, E^{10} v E^{11}. The large change stems from the change in fluorescence type, the FC% and HT% (Table 4) show a non-existent energy well overlap (FC% 0.08). This then results in a large increase of HT% (99.92%, compared to 17.95% in **3.a.**). This suggests the fluorescence increase seen in this **3.a-excitoplex** is caused by changes in the non-radiative decay process. Table 4. also shows a large change in fluorescence lifetime (k_f) in this excitoplex state with an increase of 9.68×10^{11} s^{-1*} compared to the neutral form. This means the decay process is immensely faster in anion form suggesting it may be difficult to see in standard experimental fluorescence collection, hence the emission spectrum in Figure 1b does not vary from the low concentration rations other than in intensity. This would require time-resolved fluorescence studies for formal confirmation. Figure 8c. shows that the overlap between the S_1 and S_0 wavefunctions varied in the lactone and phenoxide O(5) areas. Figure 8b, **3.c-excitoplex**, also has an intensity is increased by approximately two orders of magnitude (E^{10} v E^{12}). This is a significant increase, similarly to the **3.a-excitoplex** the FC %, it is near non-existent (0.33 %). This is reflected in Figure 8d where the $\Delta\rho$ $S_1 - S_0$ isosurface show an extremely distorted difference between the wavefunctions of S_1 and S_0. This alongside the HT % (99.67 %), suggests the **3.c-excitoplex** has enhanced fluorescence also because of changes in the excitation and deexcitation pathway. The k_f for the 3.c-excitoplex is also dramatically faster 2.46 $\times 10^{11}$ s^{-1*}, compared to the neutral form. Once again, this suggests in the excitoplex form, standard fluorescence experiments may not be able to identify changes in the emission profile, however, the rapidly reactive fluorescence is suggesting that more excitation energy is required in the movement from ground-state to excited state of the anion forms. The increase in HT% suggests the excitation point of excitoplex forms at high concentrations of 2-MIM are caused by the fluorescence pathway being *via* vibronic coupling based on movement of the transition dipole enhancement. This has been

seen previously in other fluorophores where the vibronic coupling modulated the fluorescence, usually increased by significant modulation of lactone fragment. [51, 52]

When reviewing the excitoplexes $\Delta\rho$ $S_1 - S_0$ isosurfaces 6c and d compared to Figure 8, it is seen that the lactone fragment of the oxocoumarin is more displaced between S_0 and S_1. The lactone section of the fluorophore has been found to have C=O bond stretching and ring-opening in the excited state when in a polar solvent or in response to a modulating species, which led to changes in the non-radiative decay process. [35, 21] As 2-MIM and water were both used in the experimental fluorescence study, the accompanying ^{1}H NMR data suggest that at an increased 2-MIM concentration, thus increase pH environments causes the phenoxide state occurs. This causes the excitation pathway to change as it is exciting the phenoxide equivalent rather than the fluorophore.[35] Exciting the phenoxide equivalent results in a more demanding energy pathway for exciting between S_0 and S_1 reflected by the large redshift (53 nm) seen in Figure 1a. The reason for this more demanding energy requirement is to excite the lactone fragment, rather than the oxocoumarin as a whole. This is seen when comparing the $\Delta\rho$ $S_1 - S_0$ isosurfaces of **3.a.** and **3.a-excitoplex**, (Figure 6c v Figure 8c), the anion form of the fluorophores EDD differences across the excited state and ground state wavefunction is localised in the lactone region and phenoxide O(5). This indicates the variation in EDD is caused by the lactone undergoing significant geometrical strain or even bond breaking between $S_0 \rightarrow S_1$ as seen in Krauter *et al.* work.[52] Then upon deexcitation the lactone fragment is rapidly reconfigured to the ground state shown by the increased speed of fluorescence decay, but at the same time, it results in an immensely larger emission of fluorescence. In turn, it is seen that the modification of the crystal geometry of (**3**) based on ^{1}H NMR data can aid in the correlation of the changed fluorescence properties seen in the high concentration 2-MIM compared to the fluorophore seen experimentally.

Table 4: Selected fluorescence properties from the ORCA_ESD calculations for the excitoplex states of 3.a. and 3.c.

Compound	**Adiabatic Energy Difference** cm^{-1} / nm	**Fluorescence Rate Constant** (s^{-1*})	Franck-Condon %	Herzberg-Teller %
3.a excitoplex	25434 / 393.17	9.69×10^{11}	0.08	99.92
3.c excitoplex	25341 / 394.62	2.47×10^{11}	0.33	99.67

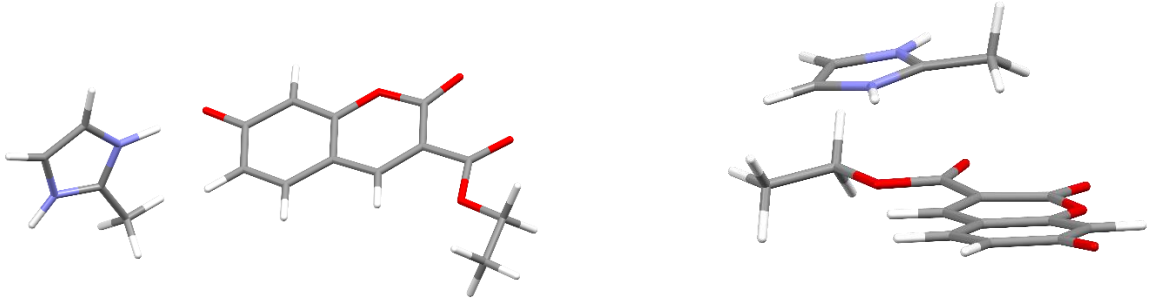

(a)

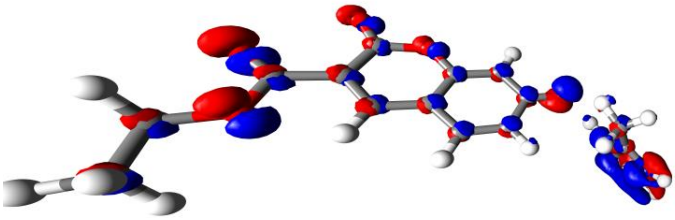

(b)

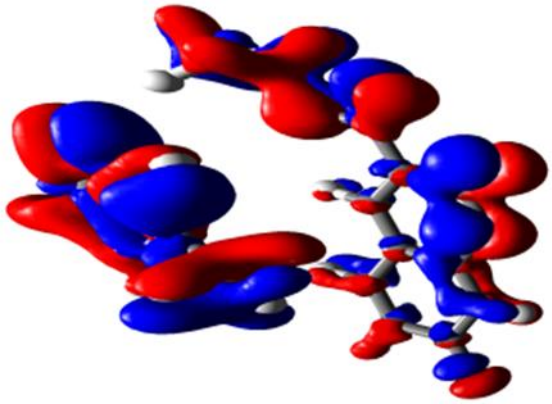

(c)

(d)

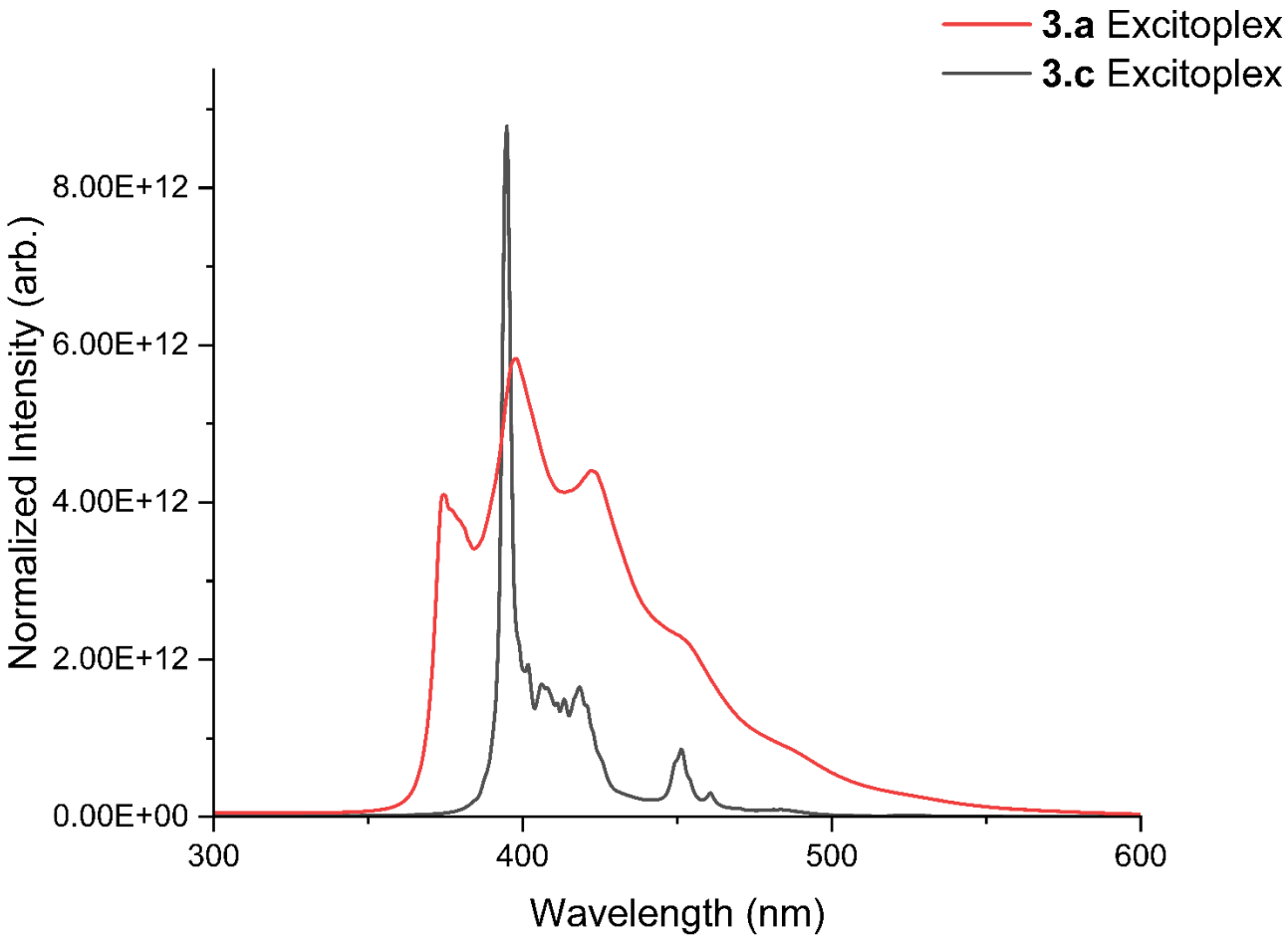

(e)

Figure 8: (a) and (b) theoretical excitoplex states of (**3.a**) and (**3.c**), respectively. (c) and (d) $\Delta\rho$ $S_1 - S_0$ isosurfaces of theoretical excitoplex states of (**3.a**) and (**3.c**), respectively, Plotted at $\pm$ 0.05e, positive e changes represent in red, negative changes represented in blue. (e) Theoretical

fluorescence spectrums of the excitoplex arrangements calculated in water using ORCA_ESD.[28, 32,45, 46]

Conclusion

Above, a study of Ethyl 7-hydroxy-2-oxo-2H-chromene-3-carboxylate hydrate, (**1**), 2-methylimdazole, (**2**), and the combined 1:1 co-crystal of Ethyl 7-hydroxy-2-oxo-2H-chromene-3-carboxylate and 2-MIM, (**3**) has been performed to ascertain how the addition of 2-MIM modulates the fluorescence of (**1**) in combination. The experimental fluorescence data indicated that combining both (**1**) and (**2**) led to reduced fluorescence with a redshift of the spectrum at concentrations ratios less than 1:10, alongside a completely different excitation profile point at a high concentration ratio 1:<10. The varied excitation profile at high concentration ratios was caused by the complete deprotonation of a fluorophore which was identified by titration of 2-MIM and (**1**) in a series of ^{1}H NMR experiments.

The results of the low concentration ranges (1:0.25-10) were explained using the computational calculations from crystalline data: the combination of crystallography and TD-DFT seems to be a novel approach. The decreased experimental fluorescence profile seen in the concentration ratios between 1:0.25-10 was caused by interfragment charge transfer between the fluorophore and 2-MIM fragments within (**3.a**). Although the proton moved minimally from the phenol O(5)-H(5) toward N(2') (0.07 Å) in (**3.a**), this resulted in a significant decrease in fluorescence caused by changes in the EDD. The changes in the EDD were seen to decrease the FC % resulting in a poor overlap of the S_1 and S_0 wavefunction, resulting in the decreased fluorescence.

To explore the different excitation profiles of the fluorophore seen experimentally modification the crystal geometry of (**3**) was made based on the ^{1}H NMR data to resemble excitoplex anion forms of 3.a. and 3.c. (based on the work of Amusoro *et al*.) led to an understanding of the effects of 2-MIM at high concentration ratios (>1:10).[5] It was seen that at these concentrations the fluorophore's fluorescence profile is dramatically changed to vibronic coupling. This suggested that in the excited state the lactone ring undergoes stretching and/or breaking to cause a significant increase in fluorescence created by the movement of the transition dipole moment. These results follow other photoacid studies, however, the methods used here were less experimentally and computationally demanding due to the novel combination of crystallography and TD-DFT. As such, this information is of interest to the fields of crystal engineering and spectroscopy, whereby, it may aid in designing and enhancing fluorophores at a low cost. Further work should be performed, with a review of excited-state charge density crystallography to formalise these results.

Acknowledgements

The authors would like to acknowledge the Gadigal people of the Eora Nation as traditional custodians of the land upon where we work, and where this research was conducted. All authors pay their respects to Elders past, present and emerging. E.N, F.L and B.A.H would like to thank The University of Sydney for scholarships.

1. K. N. Venugopala, V. Rashmi and B. Odhav, *Biomed Res. Int.*, 2013, **2013**, 963248.

2. Y.-Y. Huang, L. Chen, G.-X. Ma, X.-D. Xu, X.-G. Jia, F.-S. Deng, X.-J. Li and J.-Q. Yuan, *Molecules*, 2021, **26**, 4563.

3. J. Hirsh, J. E. Dalen, D. R. Anderson, L. Poller, H. Bussey, J. Ansell and D. Deykin, *CHEST*, 2001, **119**, 8S-21S.

4. L. Váradi, D. E. Hibbs, S. Orenga, M. Babolat, J. D. Perry and P. W. Groundwater, *RSC Adv.*, 2016, **6**, 58884-58889.

5. G. Amoruso, V. C. A. Taylor, M. Duchi, E. Goodband and T. A. A. Oliver, *J. Phys. Chem. B.* , 2019, **123**, 4745-4756.

6. M. Chakraborty, S. Bardhan, S. K. Saha and A. K. Panda, *Spectrochim*, 2012, **97**, 722-727.

7. Y. Xie, L. Yan and J. Li, *Appl. Spectrosc*, 2019, **73**, 794-800.

8. X. Tang, Z. Zhu, R. Liu, L. Ni, Y. Qiu, J. Han and Y. Wang, *Spectrochim*, 2019, **211**, 299-305.

9. R. K. Singh, T. Mandal, N. Balasubramanian, G. Cook and D. Srivastava, *Anal. Biochem.*, 2011, **408**, 309-315.

10. M. Wang, X. Wang, X. Li, Z. Yang, Z. Guo, J. Zhang, J. Ma and C. Wei, *Spectrochim*, 2020, **230**, 118075.

11. S. Hammes-Schiffer, *PNAS*, 2011, **108**, 8531.

12. J. T. Hynes, T.-H. Tran-Thi and G. Granucci, *J. Photochem. Photobiol. A*, 2002, **154**, 3-11.

13. S. Hammes-Schiffer, *J. Phys. Chem*, 2011, **2**, 1410-1416.

14. A. Kabalnov, *J Dispers Sci Technol*, 2001, **22**, 1-12.

15. R. Van Santen, *J. Phys. Chem*, 1984, **88**, 5768-5769.

16. P. W. Voorhees, *J. Stat. Phys.*, 1985, **38**, 231-252.

17. A. Lüttge, *J Electron Spectros Relat Phenomena*, 2006, **150**, 248-259.

18. D. N. Chin, G. T. R. Palmore and G. M. Whitesides, *J. Am. Chem. Soc.*, 1999, **121**, 2115-2122.

19. J. N. H. Reek, J. A. A. W. Elemans, R. de Gelder, P. T. Beurskens, A. E. Rowan and R. J. M. Nolte, *Tetrahedron*, 2003, **59**, 175-185.

20. R. Dubey, M. S. Pavan, T. N. Guru Row and G. R. Desiraju, *IUCrJ*, 2014, **1**, 8-18.

21. A. Chowdhury, S. Dasgupta and A. Datta, *Chemical Physics Impact*, 2021, **3**, 100057.

22. U. Raucci, M. G. Chiariello and N. Rega, *J. Chem. Theory*, 2020, **16**, 7033-7043.

23. R. Blessing, *J. Appl. Crystallogr*, 1997, **30**, 421.

24. G. M. Sheldrick, *Acta Crystallogr., Sect. A: Found. Crystallogr.*, 2008, **64**, 112-122.

25. F. H. Allen, O. Kennard, D. G. Watson, L. Brammer, A. G. Orpen and R. Taylor, *J. Chem. Soc., Perkin Trans. 2*, 1987, S1-S19.

26. M. Frisch, G. Trucks, H. B. Schlegel, G. Scuseria, M. Robb, J. Cheeseman, G. Scalmani, V. Barone, B. Mennucci and G. Petersson, *Inc., Wallingford, CT*, 2009, **200**.

27. F. Neese, F. Wennmohs, U. Becker and C. Riplinger, *J. Chem. Phys.*, 2020, **152**, 224108.

28. C. F. Macrae, I. Sovago, S. J. Cottrell, P. T. A. Galek, P. McCabe, E. Pidcock, M. Platings, G. P. Shields, J. S. Stevens, M. Towler and P. A. Wood, *J. Appl. Crystallogr.*, 2020, **53**, 226-235.

29 J.-D. Chai and M. Head-Gordon, *Phys. Chem. Chem. Phys*, 2008, **10**, 6615-6620.

30. A. Schäfer, C. Huber and R. Ahlrichs, *J. Chem. Phys.*, 1994, **100**, 5829-5835.

31. A. D. Becke, *J. Chem. Phys.*, 1997, **107**, 8554-8560.

32. B. de Souza, F. Neese and R. Izsák, *J. Chem. Phys.*, 2018, **148**, 034104-034104.

33. V. Barone and M. Cossi, *J. Phys. Chem. A.*, 1998, **102**, 1995-2001.

34. C. Ritter, N. Nett, C. G. Acevedo-Rocha, R. Lonsdale, K. Kräling, F. Dempwolff, S. Hoebenreich, P. L. Graumann, M. T. Reetz and E. Meggers, *Angew. Chem. Int. Ed. A...* 2015, **54**, 13440-13443.

35. D. W. Fink and W. R. Koehler, *Anal. Chem.*, 1970, **42**, 990-993.

36. J. Bezençon, M. B. Wittwer, B. Cutting, M. Smieško, B. Wagner, M. Kansy and B. Ernst, *J. Pharm. Biomed*, 2014, **93**, 147-155.

37. E. Pidcock and W. D. S. Motherwell, *Cryst. Growth*, 2004, **4**, 611-620.

38. L. J. Farrugia, *J. Appl. Crystallogr.*, 2012, **45**, 849-854.

39. B. d. Souza, F. Neese and R. Izsák, *J. Chem. Phys.*, 2018, **148**, 034104.

40. M. W. Legenza and C. J. Marzzacco, *J. Chem. Educ.*, 1977, **54**, 183.

41. M. Toutounji, *Chem. Phys.*, 2019, **523**, 205-210.

42. R. Simkovitch, L. Pinto da Silva, J. C. G. Esteves da Silva and D. Huppert, *J. Phys. Chem*, 2016, **120**, 10297-10310.

43. B. C. Westlake, M. K. Brennaman, J. J. Concepcion, J. J. Paul, S. E. Bettis, S. D. Hampton, S. A. Miller, N. V. Lebedeva, M. D. E. Forbes, A. M. Moran, T. J. Meyer and J. M. Papanikolas, *PNAS*, 2011, **108**, 8554.

44. Li, H.; Han, J.; Zhao, H.; Liu, X.; Ma, L.; Sun, C.; Yin, H.; Shi, Y., Investigation of the intermolecular hydrogen bonding effects on the intramolecular charge transfer process of coumarin 340 in tetrahydrofuran solvent. *J. Clust. Sci.* **2018,** *29* (4), 585-592.

45. Lu, T.; Chen, F., Multiwfn: a multifunctional wavefunction analyzer. *J. Comput. Chem.* **2012,** *33* (5), 580-592.

46. Guillot, B.; Viry, L.; Guillot, R.; Lecomte, C.; Jelsch, C., Refinement of proteins at subatomic resolution with MOPRO. *J. Appl. Crystallogr.* **2001,** *34* (2), 214-223.

47. Krauss, M.; Jensen, J. O.; Hameka, H. F., Electronic structure of the excited states and phenol fluorescence. *J. Phys. Chem* **1994,** *98* (40), 9955-9959.

48. Bader, R. F., *Atoms in molecules*. Wiley Online Library: 1990.

49. T. A. Keith, TK Gristmill Software, Overland Park KS, USA, 14.06.21 edn., 2014.

50. Uejima, M.; Sato, T.; Tanaka, K.; Kaji, H., Enhancement of fluorescence in anthracene by chlorination: Vibronic coupling and transition dipole moment density analysis. *Chem. Phys.* **2014,** *430*, 47-55.

51. Gibson, J.; Monkman, A. P.; Penfold, T. J., The Importance of Vibronic Coupling for Efficient Reverse Intersystem Crossing in Thermally Activated Delayed Fluorescence Molecules. *ChemPhysChem* **2016,** *17* (19), 2956-2961.

52 Krauter, C. M.; Möhring, J.; Buckup, T.; Pernpointner, M.; Motzkus, M., Ultrafast branching in the excited state of coumarin and umbelliferone. *Phys. Chem.* **2013,** *15* (41), 17846-17861.

"For Table of Contents Use Only"

Exploring The Excited-State Charge Transfer Fluorescence Profile of 7-Hydroxycoumarin and 2-Methylimidazole- A Combined X-Ray Diffraction and Theoretical Approach.

Bryson A. Hawkins, Elias Najib, Jonathan J. Du, Felcia Lai, James A. Platts, Paul W. Groundwater, and David E. Hibbs.